



# Rational amelioration of redox equilibrium by constructing hollow nanotube Co-Mn/TiO<sub>2</sub> catalyst to boost simultaneous removal of NO and Hg<sup>0</sup>

Biao Li <sup>a,b,c</sup>, Yaqin Hou <sup>b,c,\*</sup>, Jing Gao <sup>b,d</sup>, Yifan Li <sup>b,d</sup>, Bing Wang <sup>a,c</sup>, Zhanggen Huang <sup>b,d,\*</sup>, Jiancheng Wang <sup>a,c,\*\*</sup>, Liping Chang <sup>a,c</sup>, Kechang Xie <sup>a,c</sup>

<sup>a</sup> State Key Laboratory of Clean and Efficient Coal Utilization, Taiyuan University of Technology, Taiyuan 030024, PR China

<sup>b</sup> State Key Laboratory of Coal Conversion, Institute of Coal Chemistry, Chinese Academy of Sciences, Taiyuan 030001, PR China

<sup>c</sup> Key Laboratory of Coal Science and Technology, Ministry of Education and Shanxi Province, Taiyuan University of Technology, Taiyuan 030024, PR China

<sup>d</sup> University of Chinese Academy of Sciences, Beijing 100049, PR China

## ARTICLE INFO

### Keywords:

Hollow nanotube  
Oxygen vacancy  
Surface acidity  
NO  
Hg<sup>0</sup>

## ABSTRACT

Simultaneous removal of NO and Hg<sup>0</sup> in one purification unit is cost-effective, while the conflicting redox environmental requirements remains extremely challenging. Herein, hollow nanotube Co-Mn/TiO<sub>2</sub> was elaborately fabricated by reconstructing nanoparticles to ameliorate the redox equilibrium, allowing the catalysts to sustain the excellent synergistic catalytic performance, which delivered more than 98 % NO<sub>x</sub> conversion with above 95 % N<sub>2</sub> selectivity and nearly 100 % Hg<sup>0</sup> removal efficiency within 150–240 °C. Abundant oxygen vacancies and strong surface acidity were synchronously generated after the formation of unique hollow nanotube, improving the mobility of oxygen species and facilitating the adsorption and activation of reactants, and the cooperation of oxygen vacancy and surface acidity resulted in superior simultaneous removal activity. Strikingly, in situ DRIFTS and kinetic results revealed that the reaction rate was obviously accelerated on hollow nanotube Co-Mn/TiO<sub>2</sub>. This study provided new insights toward engineering efficient catalysts for simultaneous removal of NO and Hg<sup>0</sup>.

## 1. Introduction

Mercury, a highly toxic heavy metal, is a global threat to human health and environment due to its bioaccumulation, volatility and persistence [1–4]. Statistics show that coal combustion has become the major anthropogenic emission source, accounting for about 50 % of total mercury emissions in China [5]. What's more, the coal combustion process also emits lots of nitrogen oxides (NO<sub>x</sub>), leading to a series of environmental problems such as haze, acid rain and photochemical smog [6–8]. Consequently, many policies and regulations have been implemented and enormous technologies have been developed to prevent and control tailpipe pollutions of Hg<sup>0</sup> and NO<sub>x</sub> [6,9]. However, separate Hg<sup>0</sup> and NO<sub>x</sub> control technology faced the disadvantages of large footprint, high equipment and operation costs [3,9]. Hence, it is of significantly practical interest to simultaneously remove NO and Hg<sup>0</sup> in one purification unit.

Efficient simultaneous removal of NO and Hg<sup>0</sup> from flue gas remains a great challenge due to the conflicting redox environmental requirements of NO and Hg<sup>0</sup> [10]. Specifically, NO was reduced over the catalysts, while Hg<sup>0</sup> was oxidized to HgO, that is, the crucial problem to achieve the efficient removal of NO and Hg<sup>0</sup> in one purification unit is the rational amelioration of redox equilibrium. To date, significant efforts have been made to improve the reducibility to enhance the synergistic removal performance [11–15]. For instance, Li et al. [15] reported that the simultaneous removal efficiency of NO and Hg<sup>0</sup> was greatly enhanced due to the combination of copper oxides and cerium oxides enhanced the redox ability. Zhang et al. [16] doped Co and Ce in Mn@ZSM-5 catalyst to increase the ratio of Mn<sup>4+</sup> and chemisorbed oxygen, thus improving the NO and Hg<sup>0</sup> removal performance. And in our previous study [17], it was confirmed that the Co-Mn/TiO<sub>2</sub> catalysts were practicable with 90 % NO conversion and nearly 100 % Hg<sup>0</sup> removal in the temperature range of 150–240 °C, which was due to the

\* Corresponding authors at: State Key Laboratory of Coal Conversion, Institute of Coal Chemistry, Chinese Academy of Sciences, Taiyuan 030001, PR China.

\*\* Corresponding author at: State Key Laboratory of Clean and Efficient Coal Utilization, Taiyuan University of Technology, Taiyuan 030024, PR China.

E-mail addresses: [houyaqin@sxicc.ac.cn](mailto:houyaqin@sxicc.ac.cn) (Y. Hou), [zghuang@sxicc.ac.cn](mailto:zghuang@sxicc.ac.cn) (Z. Huang), [wangjiancheng@tyut.edu.cn](mailto:wangjiancheng@tyut.edu.cn) (J. Wang).

<https://doi.org/10.1016/j.apcatb.2023.123353>

Received 27 June 2023; Received in revised form 20 September 2023; Accepted 28 September 2023

Available online 29 September 2023

0926-3373/© 2023 Elsevier B.V. All rights reserved.

strong reducibility of the catalysts resulting from the interaction of manganese and cobalt. However, the strong reducibility caused the excessive oxidation of  $\text{NH}_3$ , leading to the formation of  $\text{N}_2\text{O}$  byproduct and the low  $\text{N}_2$  selectivity. For this reason, the rational amelioration of redox equilibrium of the catalysts to obtain excellent simultaneous removal efficiency is highly desirable.

The considerations described above prompted us to appropriately decrease the redox capacity of the catalyst in order to enhance its  $\text{N}_2$  selectivity, but it is still necessary to ensure its superior removal efficiency for NO and  $\text{Hg}^0$ . On the one hand, surface acid sites are widely recognized as a pivotal role in the removal of NO. Generally, a higher level of acidity promotes the adsorption and activation of  $\text{NH}_3$  on the catalysts, leading to an increased number of adsorbed  $\text{NH}_3$  species that react with gas-phase NO or adsorbed  $\text{NO}_x$  species, thus improving the removal efficiency of NO [18,19]. On the other hand, for the catalytic oxidation of  $\text{Hg}^0$ , relevant investigations have indicated that excellent  $\text{Hg}^0$  removal activity requires an increased presence of reactive oxygen species, and the introduction of oxygen vacancies into metal oxides represents an effective strategy for promoting the formation of more reactive oxygen species [20]. Zhao et al. [21] demonstrated that  $\text{MoO}_3$ -adjusted  $\delta\text{-MnO}_2$  nanosheet promoted a high concentration of oxygen vacancies, which facilitated the catalytic oxidation of  $\text{Hg}^0$  to  $\text{Hg}^{2+}$ . Based on the foregoing, the efficient simultaneous removal of NO and  $\text{Hg}^0$  with desired  $\text{N}_2$  selectivity can be concurrently achieved via improving surface acidity and oxygen vacancies of catalyst without increasing the redox capacity, which is an effective strategy to ameliorate the redox equilibrium and enhance the synergistic removal performance of the catalyst.

It has been demonstrated that the morphology of catalyst played a crucial role in the catalytic performance, and the confinement effect of specific structures can effectively regulate the oxidation state of active sites [22–26]. Among them, nanotube materials have garnered significant attention in the field of heterogeneous catalysis due to their unique properties. The nanoscale spatial confinement within hollow nanotube structure affects the mass transfer and flow rate of gas reactants, eventually altering the kinetics of various redox reactions, which is an emerging engineering approach for the regulation of redox strength [27–31]. Additionally, the unique nanotube structure has a large specific surface area to expose more active sites. Sun et al. [32] creatively designed the hollow tubular  $\text{Ce}_x\text{Sr}_{1-x}\text{TiO}_3$  catalysts could efficiently destructed chlorobenzene, which benefited from the tunable surface acidity and oxygen species mobility. Ye et al. [33] purposely tailored  $\text{MnCe}/\text{TNT}$  (titania nanotube) catalysts synchronously generating strong Lewis acidity and oxygen vacancies to enhance the performance of simultaneous catalytic removal of toluene and NO. Therefore, the precise regulation of unique hollow nanotube structure for the catalysts to achieve the purpose of ameliorating the redox equilibrium on the basis of increasing surface acidity and oxygen vacancies is feasible and innovative research.

Herein, a series of hollow nanotube Co-Mn/TiO<sub>2</sub> catalysts were elaborately synthesized through the reconstruction of Co-Mn/TiO<sub>2</sub> nanoparticles using hydrothermal method. The structure-activity relationship of hollow nanotube Co-Mn/TiO<sub>2</sub> was systematically investigated by performance evaluation experiments in conjunction with physicochemical properties. Moreover, the in situ diffuse reflectance infrared transform spectroscopy (DRIFTS) and kinetic studies were performed to unravel the synergistic removal reaction mechanism over the hollow nanotube Co-Mn/TiO<sub>2</sub> catalysts. Overall, this work was expected to be a strategy for the further design of synergistic removal catalysts with excellent activity, which opens a new path for simultaneous catalytic NO and  $\text{Hg}^0$  elimination.

## 2. Experimental section

### 2.1. Catalyst preparation

The Co-Mn/TiO<sub>2</sub> nanoparticles catalysts were prepared by sol-gel method in our previous work [17], and the catalysts were denoted as CMT in this work. The hollow nanotube Co-Mn/TiO<sub>2</sub> catalysts were synthesized using hydrothermal method. Firstly, 0.8 g CMT was added to 40 mL NaOH (10 mol L<sup>-1</sup>) solution followed by ultrasound for 1 h. Then, the solution was poured into a Teflon-lined stainless autoclave and hydrothermally treated at 150 °C for 24 h. After the reactor was cooled down to room temperature, the precipitate was isolated by centrifugation and flushed with deionized water and 0.1 mol L<sup>-1</sup> HNO<sub>3</sub> successively, and then washed with deionized water and anhydrous ethanol several times. Finally, the hollow nanotube Co-Mn/TiO<sub>2</sub> was obtained after dried at 80 °C and calcined in air at 400 °C for 2 h, which was labeled as CMT-NT. In addition, the hollow nanotube Co-Mn/TiO<sub>2</sub> was also synthesized through the same method while the cetyl trimethyl ammonium bromide (CTAB) was added into NaOH solution and was denoted as CMT-NT-C.

### 2.2. Catalytic performance evaluations

The synergistic removal performance tests for NO and  $\text{Hg}^0$  were conducted using 0.2 g of catalyst (40–60 mesh) in a fixed-bed quartz reactor with a 6 mm inner diameter. The schematic of experimental device is shown in Fig. S1, the constituents of simulated flue gas were 500 ppm NO, 500 ppm  $\text{NH}_3$ , 5 % O<sub>2</sub>, 115 µg/m<sup>3</sup>  $\text{Hg}^0$ , 5 % H<sub>2</sub>O, 50 ppm SO<sub>2</sub> (when used) and balanced N<sub>2</sub>, the total flow rate was 200 mL/min, corresponding to a space velocity of 60,000 mL g<sup>-1</sup> h<sup>-1</sup>. The concentrations of  $\text{Hg}^0$ , NO, NO<sub>2</sub>, N<sub>2</sub>O, and  $\text{NH}_3$  were monitored by an online RA-915 Mercury Analyzer (Lumex Ltd, Russia) and a DX4000 FT-IR gas analyzer (Gaset Technologies Crop), respectively. The  $\text{Hg}^0$  removal efficiency ( $E_{\text{Hg}^0}$ ), NO<sub>x</sub> conversion efficiency ( $E_{\text{NO}_x}$ ), and N<sub>2</sub> selectivity were calculated according to the following expressions:

$$E_{\text{Hg}^0} = \frac{\text{Hg}_{\text{in}}^0 - \text{Hg}_{\text{out}}^0}{\text{Hg}_{\text{in}}^0} \quad (1)$$

$$E_{\text{NO}_x} = \frac{[\text{NO}_x]_{\text{in}} - [\text{NO}_x]_{\text{out}}}{[\text{NO}_x]_{\text{in}}} \quad (2)$$

$$\text{N}_2 \text{ selectivity} = \frac{[\text{NO}_x]_{\text{in}} + [\text{NH}_3]_{\text{in}} - [\text{NO}_x]_{\text{out}} - [\text{NH}_3]_{\text{out}} - 2[\text{N}_2\text{O}]_{\text{out}}}{[\text{NO}_x]_{\text{in}} + [\text{NH}_3]_{\text{in}} - [\text{NO}_x]_{\text{out}} - [\text{NH}_3]_{\text{out}}} \times 100\% \quad (3)$$

The  $\text{NH}_3$  oxidation were also conducted in the fixed-bed quartz reactor containing 500 ppm  $\text{NH}_3$ , 5 % O<sub>2</sub>, and balanced N<sub>2</sub>. The conversion of  $\text{NH}_3$  was determined as follows:

$$\text{NH}_3 \text{ conversion} = \frac{[\text{NH}_3]_{\text{in}} - [\text{NH}_3]_{\text{out}}}{[\text{NH}_3]_{\text{in}}} \quad (4)$$

The reaction rates of NO and  $\text{Hg}^0$  were measured under kinetic conditions where both internal and external diffusion were excluded (conversion rate was less than 30 %). And the kinetic parameters for NO conversion were evaluated under the assumption that the reaction was considered to be a first-order reaction. The apparent activation energy ( $E_a$ ) was calculated through the Arrhenius law:

$$r = \frac{F \times X}{m} \quad (5)$$

$$r = kc = A \exp\left(-\frac{E_a}{RT}\right) \quad (6)$$

where  $r$ ,  $F$ ,  $X$ ,  $m$ ,  $k$ ,  $c$ ,  $A$ ,  $E_a$ ,  $R$ , and  $T$  are the reaction rate (mol g<sup>-1</sup> s<sup>-1</sup>),

gas flow rate ( $\text{mol s}^{-1}$ ), conversion efficiency, catalyst weight (g), rate constant ( $\text{mL g}^{-1} \text{s}^{-1}$ ), concentration of species ( $\text{mol mL}^{-1}$ ), pre-exponential factor, apparent activation energy ( $\text{kJ mol}^{-1}$ ), universal gas constant ( $\text{J mol}^{-1} \text{K}^{-1}$ ), and reactor temperature (K), respectively.

The turnover frequency (TOF) of NO and  $\text{Hg}^0$  was estimated on an active center of manganese or cobalt by the following equation:

$$\text{TOF} = \frac{F \times X \times M}{m \times \omega} \quad (7)$$

where M is the molar mass and  $\omega$  represents the surface element content

calculated by the XPS results.

### 2.3. Catalyst characterization

The prepared catalysts were characterized by X-ray diffraction (XRD), transmission electron microscopy (TEM), nitrogen absorption-desorption, Raman spectroscopy, inductively coupled plasma optical emission spectroscopy (ICP-OES), hydrogen temperature programmed reduction ( $\text{H}_2$ -TPR), oxygen temperature programmed desorption ( $\text{O}_2$ -TPD), electron paramagnetic resonance (EPR), X-ray photoelectron

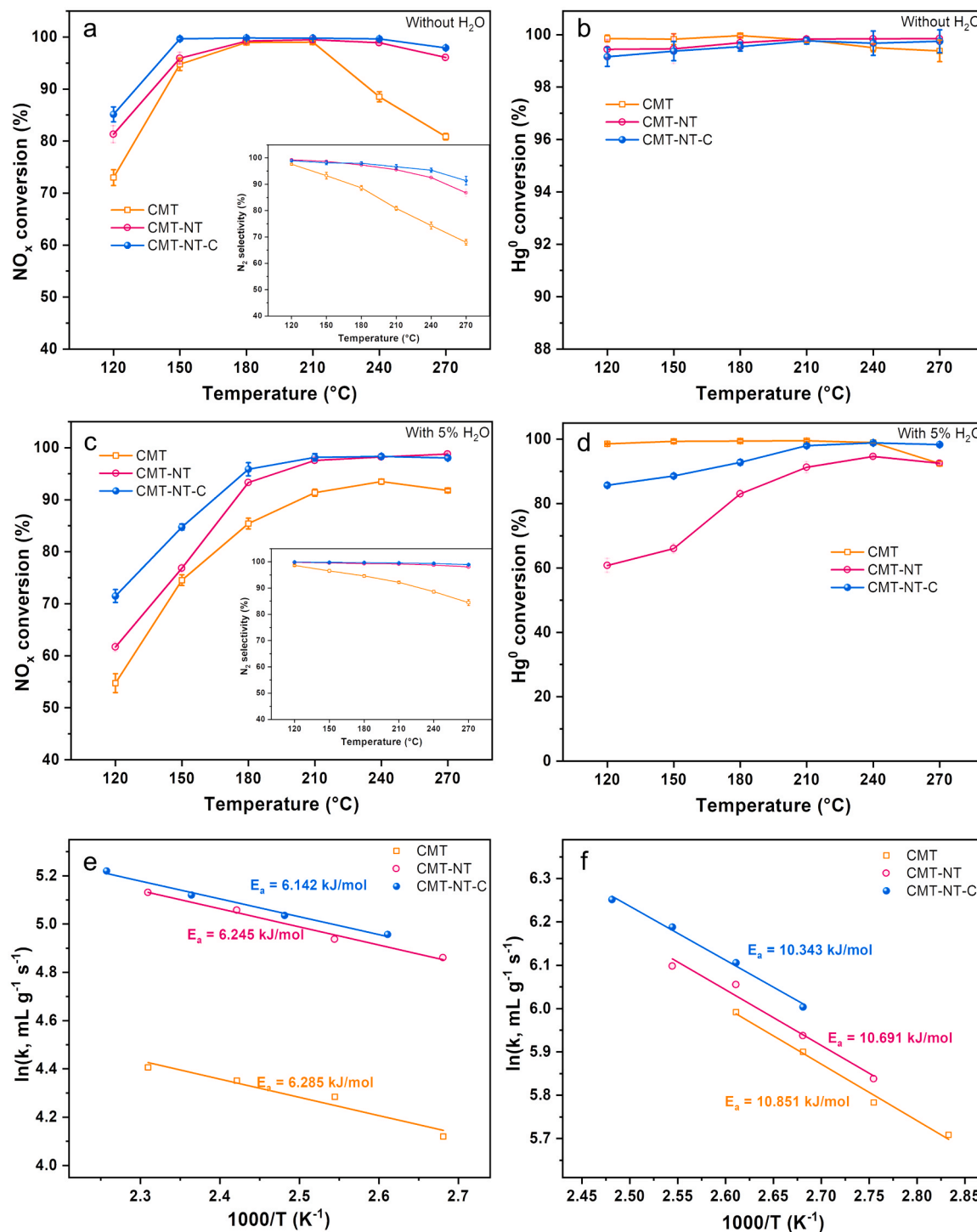


**Fig. 1.** NO conversion efficiency (a, c) and  $\text{Hg}^0$  removal efficiency (b, d) as a function of the reaction temperature for the simultaneous removal reaction in the absence or the presence of  $\text{H}_2\text{O}$ . Arrhenius plots of NO reduction (e) and  $\text{Hg}^0$  oxidation (f).

spectroscopy (XPS), temperature programmed desorption of  $\text{NH}_3$  ( $\text{NH}_3$ -TPD), pyridine-infrared spectra (Py-IR), temperature programmed desorption of  $\text{Hg}^0$  ( $\text{Hg}$ -TPD), and in situ diffuse reflectance infrared transform spectroscopy (in situ DRIFTS). More characterization details are provided in the [Supplementary Material](#).

### 3. Results and discussion

#### 3.1. Catalytic performance of simultaneously remove NO and $\text{Hg}^0$

The simultaneous removal efficiency of NO and  $\text{Hg}^0$  over the catalysts as a function of temperature was shown in Fig. 1(a, b). The CMT-NT-C exhibited the best simultaneous removal performance relative to that of the other catalyst, exhibiting above 98 %  $\text{NO}_x$  conversion and nearly 100 %  $\text{Hg}^0$  removal efficiency in the range of 150–240 °C, suggesting that the hollow nanotube structure can effectively promote the simultaneous removal activity of NO and  $\text{Hg}^0$ . Intriguingly, the  $\text{N}_2$  selectivity was improved significantly of the CMT-NT-C catalysts over the whole temperature window, amounting to 98 % at 180 °C, which further indicated that the hollow nanotube structure shows much better simultaneous removal performance than nanoparticles, this conclusion is also in line with our expectations. In the practical application, the industrial flue gas often contains certain amounts of water vapor, thus it is necessary to add  $\text{H}_2\text{O}$  into the activity test. As shown in Fig. 1(c, d), the simultaneous removal efficiency of the catalyst decreased to varying degrees in the presence of 5 %  $\text{H}_2\text{O}$ , the inhibition effect was more obvious especially at low temperature region ( $\leq 180$  °C), which was mainly attributed to the competitive adsorption between  $\text{H}_2\text{O}$  and reactant molecules [17]. However, the inhibitory effect of  $\text{H}_2\text{O}$  for NO removal weakened gradually with the increase of reaction temperature, and the  $\text{Hg}^0$  conversion efficiency of the CMT slightly decreased due to part of  $\text{HgO}$  decomposed when the temperature above 240 °C, while the CMT-NT-C catalyst still had excellent  $\text{Hg}^0$  removal efficiency at 270 °C due to the abundant surface reactive oxygen species on the catalyst surface. And the  $E_{\text{NO}_x}$  and  $E_{\text{Hg}^0}$  reached 95 % and 98 % over the

CMT-NT-C catalysts at 180 °C, substantiating its satisfied water resistance. Additionally, the stability and reusability test were investigated in Fig. S11 and Fig. S12, and the results indicated the hollow nanotube catalyst had superior stability and reusability.

In order to reflect the effect mechanism of the morphology and structure on the performance, the kinetic studies were performed and the results being given in Fig. 1(e, f). It can be clearly seen that the CMT-NT-C exhibited the lowest apparent activation energy ( $E_{a\text{NO}} = 6.142 \text{ kJ mol}^{-1}$ ,  $E_{a\text{Hg}^0} = 10.343 \text{ kJ mol}^{-1}$ ) for both NO and  $\text{Hg}^0$  conversion, demonstrating that the simultaneous removal of NO and  $\text{Hg}^0$  on the CMT-NT-C surface could proceed with lower energy barrier. Moreover, the relative TOF values were also calculated and presented in Fig. S2. Among them, the CMT-NT-C possessed the highest TOF values in simultaneous removal of NO and  $\text{Hg}^0$  whether surface manganese or cobalt was the active site, which is in agreement with the catalytic activity. And the TOF and reaction rate was compared with the reported literature shown in Table S5, it was found that the hollow nanotube structure Co-Mn/ $\text{TiO}_2$  possessed higher TOF or reaction rate. The abovementioned results clearly demonstrate that the formation of hollow nanotube structure Co-Mn/ $\text{TiO}_2$  possessed superior simultaneous removal performance for NO and  $\text{Hg}^0$ .

#### 3.2. Structural properties

The morphology and the microstructure of the catalysts were revealed by TEM and HRTEM as displayed in Fig. 2(a-d) and Fig. S3. It was observed that the CMT catalysts presented irregular aggregation of nanoparticles, and the hollow nanotube structure had initially formed for the CMT-NT as shown in Fig. S3, but some accumulation of nanoparticles was still clearly observed on the surface of hollow nanotube. When the surfactant CTAB was introduced in the hydrothermal process, the uniform hollow nanotube structure was successfully obtained with about 9.6 nm outer diameter and 4.2 nm inner diameter as shown in Fig. 2c. This hollow nanotube structure has abundant internal pore space, which can provide more active sites for the reactant molecular

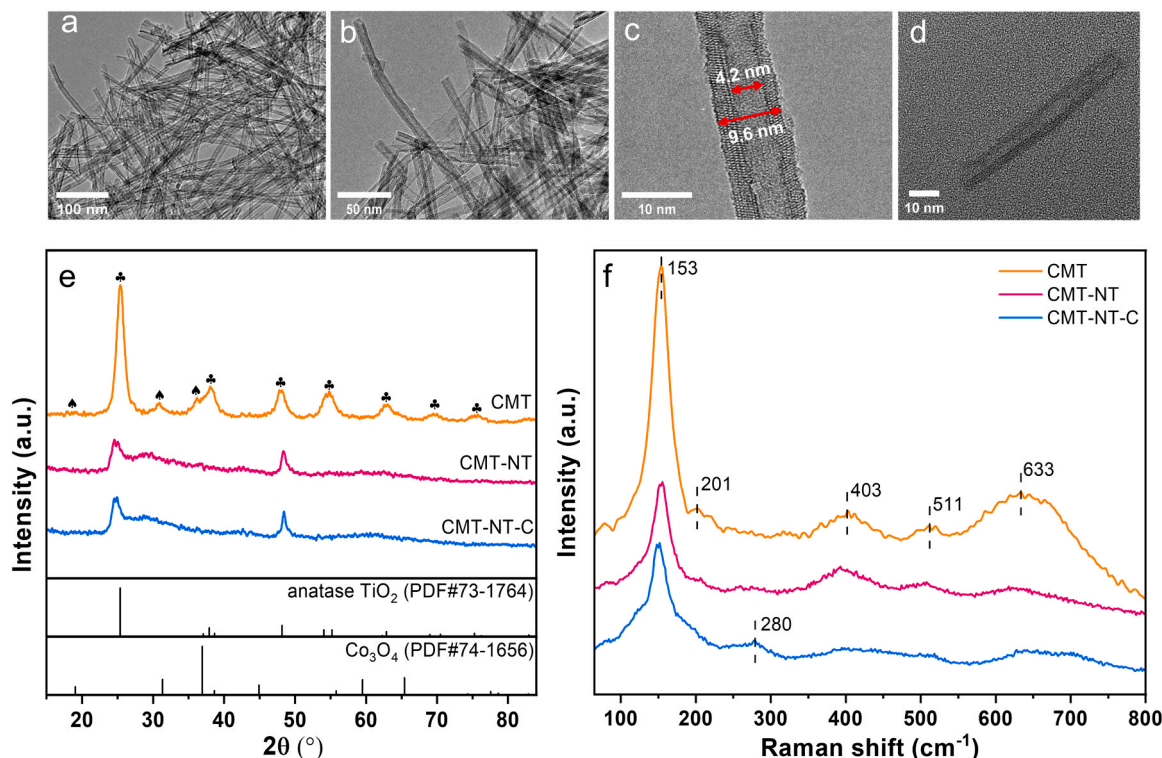


Fig. 2. The TEM images of the CMT-NT-C (a, b), and HRTEM image of the CMT-NT-C (c, d). XRD patterns (e) and Raman spectra (f) of the catalysts.



reaction. At the same time, the unique hollow nanotube structure catalysts could enhance the interaction between the reactant molecules and the catalyst surface and eventually alter the kinetics of each reaction, which improve the overall catalytic performance [29,34]. Therefore, the CMT-NT-C shown excellent synergistic removal activity for NO and Hg<sup>0</sup>.

To gain more insights into the structural features of the prepared catalysts, XRD patterns and Raman spectra were used to characterize the crystal structure. As illustrated in Fig. 2e, all of the catalysts show major diffraction peaks of anatase-phase TiO<sub>2</sub>, and the diffraction peaks of Co<sub>3</sub>O<sub>4</sub> were only found on CMT, suggesting the excellent dispersibility or an amorphous state of Mn and Co species over CMT-NT-C. It can also be observed that the intensity of anatase-phase TiO<sub>2</sub> was much weaker after the formation of hollow nanotube, which implied that the hollow nanotube possessed a confinement effect on the crystallization of the catalysts. Furthermore, the Raman spectra results were analyzed as a complement to XRD results. As shown in Fig. 2f, the obvious peaks emerged at 153, 201, 403, 511, and 633 cm<sup>-1</sup> were assigned to the anatase-phase TiO<sub>2</sub> in CMT [6,35], in accordance with the XRD results, the peaks intensity decreased significantly over CMT-NT-C, implying the poor crystallinity. Notably, the peak at 633 cm<sup>-1</sup> ascribed to the vibration Ti-O-Ti weakened while the peak at 280 cm<sup>-1</sup> ascribed to the vibration of Ti-O-H appeared on CMT-NT-C, demonstrating the destruction of the Ti-O-Ti structure and the formation of Ti-O-H over hollow nanotube Co-Mn/TiO<sub>2</sub>, which could provide abundant surface acid sites for the catalysts [19,35].

The N<sub>2</sub> physisorption results of the prepared catalysts were displayed in Fig. S4 and Table 1. The three catalysts all showed representative type-IV isotherms, suggesting the existence of uniform mesoporous structure. In addition, the specific surface area of CMT-NT-C (296 m<sup>2</sup>/g) was much larger than that of CMT (146 m<sup>2</sup>/g), which was mainly caused by the formation of hollow nanotube structure. The large specific surface area is conducive to facilitate the adsorption of reactant molecules and expose more active sites.

Furthermore, the ICP-OES data was shown in Table 1 to validate the element compositions of the catalysts. The ratio of Mn and Co for CMT-NT-C (6.63 wt %, 4.42 wt %) is lower than the CMT (10.58 wt %, 5.39 wt %), indicating that a small amount of Mn and Co was lost during the hydrothermal process.

### 3.3. Surface chemical status

The XPS analysis were conducted to deeply investigate the surface chemical states of the catalysts, as for Fig. 3, and the surface relative proportion was quantitatively calculated and listed in Table S2. As shown in Fig. 3a, the spin-orbital coupling peak of Mn 2p was composed of three subpeaks corresponding to Mn<sup>4+</sup> (644.1–644.5 eV), Mn<sup>3+</sup> (641.7–642.0 eV), and Mn<sup>2+</sup> (640.1–640.6 eV), respectively [36]. The ratio of Mn<sup>3+</sup>/(Mn<sup>4+</sup> + Mn<sup>3+</sup> + Mn<sup>2+</sup>) of CMT-NT-C (70.3 %) was higher than that of CMT (63.4 %) and CMT-NT (67.3 %), confirming the electron transfer existed in the process of forming hollow nanotube. In addition, the higher ratio of Mn<sup>3+</sup>/(Mn<sup>4+</sup> + Mn<sup>3+</sup> + Mn<sup>2+</sup>) would formed more oxygen vacancies due to the electrostatic balance, which played an important role in improving the catalytic performance [37]. In

the spectra of Co 2p, the two major peaks at 780.0–780.1 eV and 781.8–782.1 eV were assigned to the Co<sup>3+</sup> and Co<sup>2+</sup> respectively [20], and the calculated Co<sup>3+</sup>/(Co<sup>2+</sup> + Co<sup>3+</sup>) ratios of CMT, CMT-NT, and CMT-NT-C were 49.3 %, 51.1 %, and 52.7 %, respectively. It further demonstrated that the strong electron transfer resulted from the confinement effect of hollow nanotube structure occurred on the catalysts, which regulated the redox capability of the catalysts.

As shown in Fig. 3(c), the O 1s spectra of the prepared catalysts consisted of three peaks at around 532.0–532.6 eV, 530.8–531.2 eV, and 529.6–530.0 eV, corresponding to the surface adsorbed hydrated oxide species (denoted as O<sub>sur</sub>), chemisorbed oxygen on oxygen vacancies or defect sites (denoted as O<sub>ads</sub>), and lattice oxygen (denoted as O<sub>latt</sub>), respectively [38,39]. It was distinct that the CMT-NT-C showed higher O<sub>ads</sub>/(O<sub>sur</sub> + O<sub>ads</sub> + O<sub>latt</sub>) ratio (22.7 %), which was higher than that for CMT (16.9 %) and CMT-NT (19.3 %), implying more chemisorbed oxygen was produced in the formation of hollow nanotube. Generally, the generation of O<sub>ads</sub> quickens the activation of oxygen, which is in favor of the catalytic activity [40,41]. Noteworthy, the peak of O 1s for the CMT-NT-C moved to higher binding energy than that of the CMT, indicating that lower electron cloud density of O over the CMT-NT-C, which was due to the strong interaction between Mn, Co and Ti during the formation of hollow nanotube affected the chemical environment of O, and the strong interaction was conducive to improving the catalytic activity of the CMT-NT-C. On the basis of XPS analysis, it is clear that the strong electron transfer derived from the confinement and the generation of more O<sub>ads</sub> after the formation of hollow nanotube should make a contribution to its excellent simultaneous catalytic performance of NO and Hg<sup>0</sup>.

### 3.4. Redox capability and oxygen species mobility

H<sub>2</sub>-TPR can be used to characterize the redox properties of catalysts. As illustrated in Fig. 4a, the first reduction peak located at roughly 300 °C was assigned to the reduction of Mn<sup>4+</sup> to Mn<sup>3+</sup> and the reduction peak emerged in the range of 340–400 °C was attributed to the reduction of Co<sup>3+</sup> to Co<sup>2+</sup>, while Mn<sup>3+</sup> to Mn<sup>2+</sup> and Co<sup>2+</sup> to Co<sup>0</sup> reduction produced a large, broad peak above 400 °C [18,42]. It is obvious that all reduction peak shifted to higher temperature among the CMT-NT-C, manifesting that the construction of hollow nanotube certainly declined the reducibility of catalysts. The quantitative results, summarized in Table S3, shown that the H<sub>2</sub> consumption amount over these catalysts followed the sequence of CMT (2.30 mmol g<sup>-1</sup>) > CMT-NT (2.19 mmol g<sup>-1</sup>) > CMT-NT-C (1.94 mmol g<sup>-1</sup>), implying the reducibility of the catalyst gradually decreased with the formulation of hollow nanotube, which was related to the slight loss of Mn and Co confirmed by ICP results and the decrease of Mn<sup>4+</sup> proportion confirmed by XPS results after the formation of hollow nanotube, unambiguously providing evidence that the redox capacity of the catalysts was regulated by constructing the hollow nanotube structure. Previous analysis proposed that too strong oxidation of the catalysts would lead to excessive oxidation of NH<sub>3</sub>, resulting in the decrease of NO removal efficiency and N<sub>2</sub> selectivity. Therefore, the abovementioned results can explain why the CMT-NT-C exhibited much higher NO conversion and N<sub>2</sub> selectivity than other catalysts.

The oxygen species mobility of prepared catalysts was investigated by O<sub>2</sub>-TPD. As plotted in Fig. 4b, the oxygen desorption curves were classified into three categories: physically/chemically adsorbed oxygen (labeled as α) at 100–350 °C, oxygen adsorbed on surface vacancies or surface lattice oxygen (labeled as β) at 350–600 °C, bulk lattice oxygen (labeled as γ) above 600 °C [32,43–45]. The desorption temperature of oxygen species could reflect the oxygen activation capacity of the catalysts, and the desorption peaks temperature of β (495 °C) and γ (616 °C) for the CMT-NT-C were significantly lower than that of the CMT and CMT-NT-C, indicating the activation energy of lattice oxygen decreased, and the migration of lattice oxygen to the surface was accelerated after the formation of hollow nanotube. According to the calculation results

**Table 1**  
Textural property and ICP results of the as-prepared catalysts.

Sample	BET specific surface area (m <sup>2</sup> /g)	Total volume capacity (cm <sup>3</sup> /g)	Average pore size (nm)	ICP		
				Mn (wt %)	Co (wt %)	Ti (wt %)
CMT	146	0.23	6.40	10.58	5.39	61.92
CMT-NT	287	0.45	6.29	6.86	3.54	57.65
CMT-NT-C	296	0.48	6.44	6.63	4.42	58.54

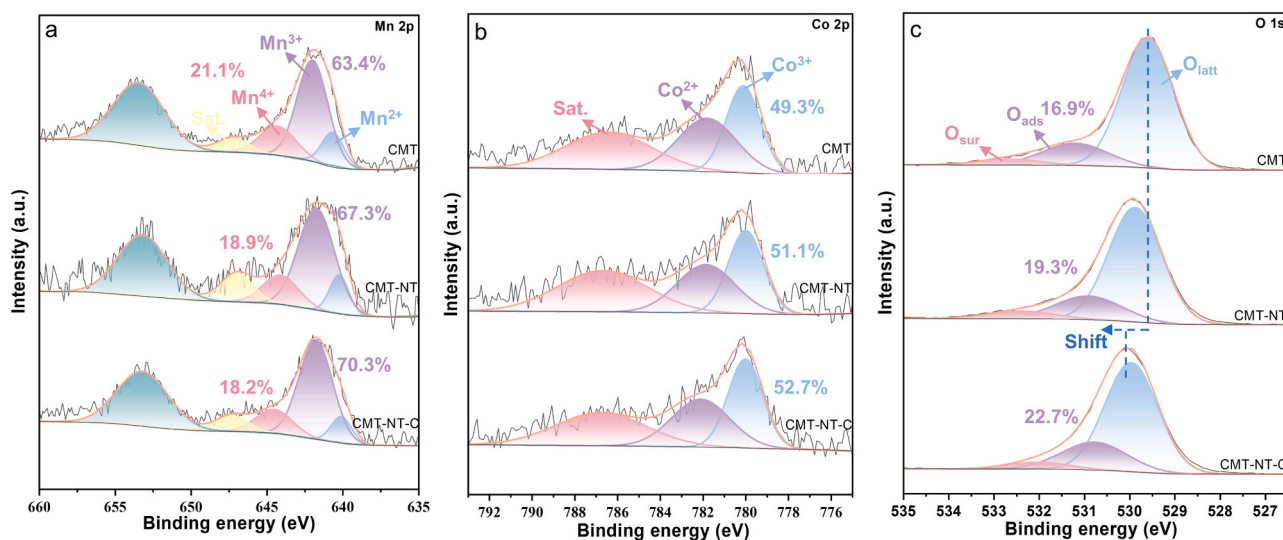


Fig. 3. XPS spectra of Mn 2p (a), Co 2p (b), and O 1s (c) regions over the as-prepared catalysts.

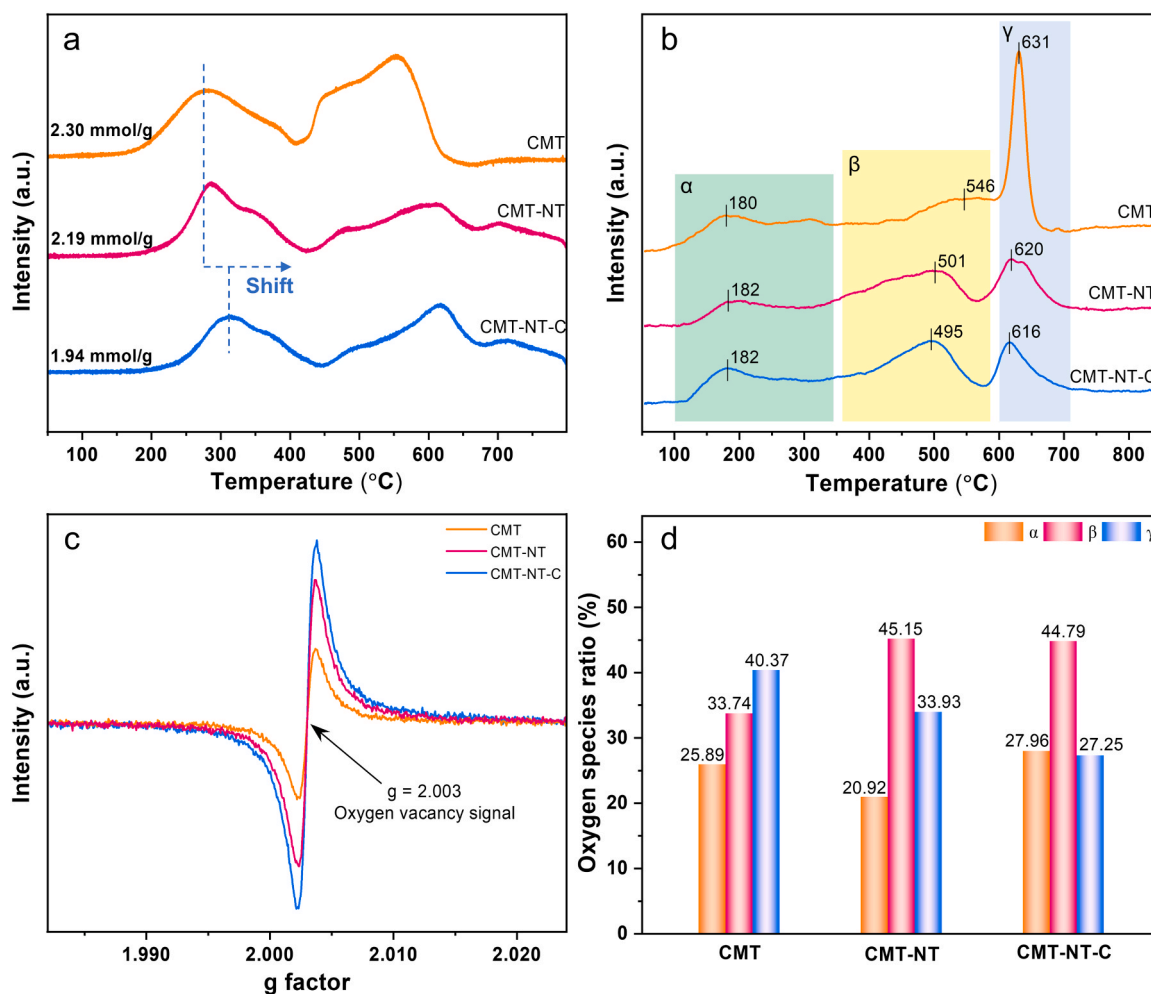


Fig. 4. H<sub>2</sub>-TPR (a), O<sub>2</sub>-TPD (b) and EPR (c) profiles of the prepared catalysts. Oxygen species ratio (d) on the catalysts.

shown in Fig. 4d, the CMT-NT-C possessed lower desorption ratio of  $\gamma$  (27.25 %) than CMT (40.37 %), which was attributed to the bulk lattice oxygen migrated to the surface to produce more surface reactive oxygen species ( $\alpha$  and  $\beta$ ) during the formation of uniform hollow nanotube,

while there was also a migration and transformation between surface reactive oxygen species (part of the surface lattice oxygen migrated to the surface physically/chemically oxygen), resulting in an increase of the  $\alpha$  oxygen species from 20.92 (in CMT-NT) to 27.96 (in CMT-NT-C).

This testified the CMT-NT-C possessed more oxygen vacancy for the migration of oxygen species. Besides, more surface reactive oxygen species ( $\alpha$  and  $\beta$ ) was beneficial to the activation of the reactants, so the CMT-NT-C exhibited the most outstanding simultaneous removal performance. These results demonstrated the hollow nanotube structure of the CMT-NT-C improved the mobility of oxygen species.

The migration oxygen species is closely related to the oxygen vacancy on the catalysts [46]. Thus, the EPR spectroscopy was further performed to accurately clarify the distribution of oxygen vacancy on the catalysts. As shown in Fig. 4c, the obvious signal at  $g = 2.003$  was observed for all catalysts, which was attributed to the signal of oxygen vacancy [47]. Indeed, this provides strong evidence to confirm the existence of oxygen vacancy in prepared catalyst. Among them, the CMT-NT-C exhibited the strongest signal intensity, suggesting that more oxygen vacancy exists in the catalysts after the construction of hollow nanotube, which is in agreement with the XPS and  $O_2$ -TPD results. And the abundant oxygen vacancy facilitated the adsorption and activation of oxygen and promoted the mobility of bulk oxygen, which accelerated the redox cycle in catalytic reaction and thus improved the catalytic performance [48]. These results were good consistent with the superior reactivity of the CMT-NT-C for the simultaneous removal of NO and  $Hg^0$ .

### 3.5. Surface acidity

$NH_3$ -TPD experiments were conducted to reveal the surface acidity of the prepared catalysts. As displayed in Fig. 5a, the desorption peak at low temperature below  $200^\circ C$  and in the temperature range of  $200$ – $500^\circ C$  corresponding the weak acid sites and middle acid sites, respectively [41,49]. It was obviously observed that the desorption of the weak acid

sites and middle acid sites over CMT-NT-C were significantly larger than those of CMT. According to the desorption areas calculation results, the CMT-NT-C exhibited higher desorption of  $NH_3$  ( $281.25 \mu mol g^{-1}$ ) than CMT ( $167.25 \mu mol g^{-1}$ ) and CMT-NT ( $234.91 \mu mol g^{-1}$ ), suggesting the hollow nanotube Co-Mn/TiO<sub>2</sub> possessed the strongest acidity and the largest amount of acid sites, which enhanced the adsorption of  $NH_3$  and thus improved the NO conversion. Moreover, the desorption peaks of  $N_2O$  and NO appeared in the temperature programed process, which was caused by the oxidation of adsorbed  $NH_3$  through surface active oxygen on the catalysts. And compared the CMT, the  $N_2O$  desorption amount of CMT-NT-C ( $20.58 \mu mol g^{-1}$ ) decreased by half, which corresponded to the increased  $N_2$  selectivity of the CMT-NT-C shown in the activity evaluation results.

Furthermore, the type of acid site was clearly analyzed by the pyridine-IR spectra shown in Fig. 5b. The band at  $1446 cm^{-1}$  was assigned to the pyridine adsorbed on Lewis acid sites and the peak at  $1540 cm^{-1}$  was ascribed to the Brønsted acid sites, while the band at  $1488 cm^{-1}$  represented both Lewis acid sites and Brønsted acid sites [18, 32,50]. And the quantified amounts were summarized in Table S3. As for the CMT-NT-C, the amount of Lewis acid sites and Brønsted acid sites was higher than that of CMT at  $50^\circ C$ , which demonstrated that the construction of hollow nanotube structure generated abundant acid sites. Additionally, the pyridine adsorption peaks at both Lewis acid sites and Brønsted acid sites reduced as the temperature increased from  $50$  to  $200^\circ C$ , while the CMT-NT-C still had stronger Lewis acid sites than that of CMT. Consequently, the CMT-NT-C with a relatively large amount of Lewis acid sites and Brønsted acid sites finally resulted in excellent adsorption performance for  $NH_3$ .

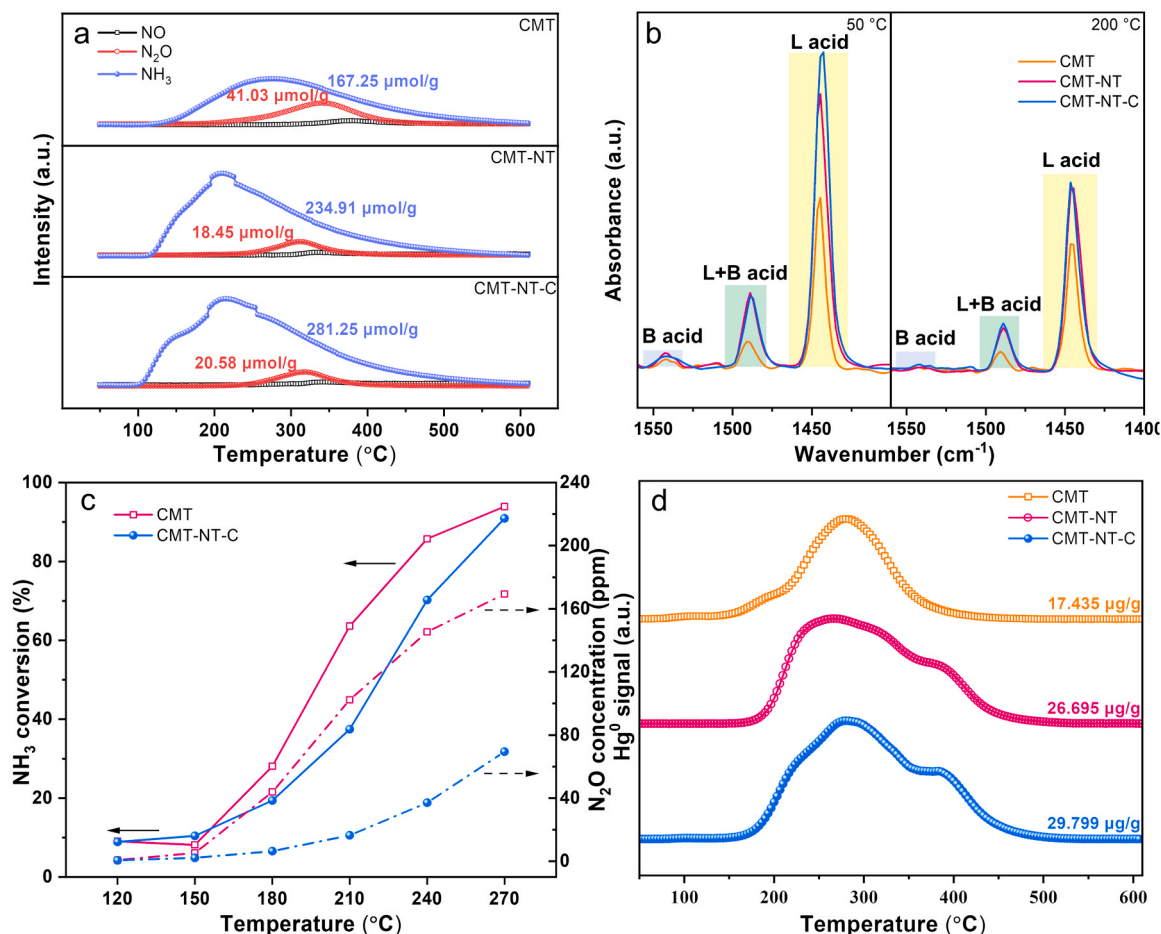


Fig. 5.  $NH_3$ -TPD profile (a) and Pyridine-IR spectra (b) of the prepared catalysts; Oxidation of  $NH_3$  (c) over CMT and CMT-NT-C,  $Hg$ -TPD profile (d) of the catalysts.

### 3.6. Reaction mechanism

The above characterization results had shown the changes in the structure and surface properties of Co-Mn/TiO<sub>2</sub> after the construction of hollow nanotube. In order to further correlate the structural characteristics with the catalytic performance, the surface reaction mechanism of the catalysts was systematically analyzed.

#### 3.6.1. Adsorption and activation of reactants

The adsorption and activation of reactants play a key role in simultaneous catalytic reaction, so the in situ DRIFTS studies of NO and NH<sub>3</sub> adsorption-desorption at different temperature were carried out, and the adsorption species on the CMT and CMT-NT-C were presented in Fig. 6. For the NO + O<sub>2</sub> adsorption-desorption, the band associated with monodentate nitrate (1508 cm<sup>-1</sup>) on the CMT-NT-C became weaker, while the band assigned to adsorbed NO<sub>2</sub> species (1618 cm<sup>-1</sup>) became stronger [51], implying that the production of monodentate nitrate was inhibited after the construction of hollow nanotube and more adsorbed NO<sub>2</sub> was formed, which was more easily to participate in the SCR reaction than monodentate nitrate [18]. When the temperature was increased, the bands corresponding to adsorbed NO<sub>2</sub>, bidentate nitrate, monodentate nitrate, linear nitrite, chelating nitrite, and bridged nitrate gradually weakened, and almost disappeared at 300 °C. As shown in Fig. 6(c,d), the NH<sub>3</sub> adsorbed on Lewis acid sites (1608 cm<sup>-1</sup>) and NH<sub>4</sub><sup>+</sup> adsorbed on Brønsted acid sites (1662 cm<sup>-1</sup>) were observed with much higher intensity over the CMT-NT-C, and the appearance of a large peak at 1445 cm<sup>-1</sup> over the CMT-NT-C was attributed to the NH<sub>4</sub><sup>+</sup> bonded to

Brønsted acid sites [7,51]. This observation demonstrated more Lewis acid sites and Brønsted acid sites were generated after the formation of the hollow nanotube structure, which was consistent with the NH<sub>3</sub>-TPD and pyridine-IR results.

To better understand the activation of reactants, NH<sub>3</sub> oxidation were investigated on the CMT and CMT-NT-C, respectively. As can be seen in Fig. 5c, the NH<sub>3</sub> oxidation reaction was inhibited by constructing hollow nanotube structure, implying less NH<sub>3</sub> was consumed by the oxidation with O<sub>2</sub> and more NH<sub>3</sub> could reacted with NO, which had a positive impact on the performance for NO removal. Simultaneously, less N<sub>2</sub>O was produced during the NH<sub>3</sub> oxidation over the CNT-NT-C, corresponding to the superior N<sub>2</sub> selectivity. The above analysis confirmed that the construction of hollow nanotube structure precisely regulated the redox capacity of the catalysts and thus enhanced its catalytic performance.

Hg-TPD experiments were conducted to study the Hg<sup>0</sup> adsorption performance, and the desorption amount was calculated by the desorption peak area. As shown in Fig. 5d, the desorption of Hg<sup>0</sup> below 200 °C was attributed to the physical adsorption and the desorption above 200 °C was caused by the breakdown of HgO [9], proving that the Hg<sup>0</sup> could reacted with active oxygen species on the catalysts surface to produce HgO. According to the calculated results, the CMT-NT-C emerged the largest Hg<sup>0</sup> desorption amount (29.799 μg g<sup>-1</sup>), which was due to the formation of hollow nanotube exposed more active sites through the larger specific surface area and produced more active oxygen species, this was conducive to the adsorption of Hg<sup>0</sup>.

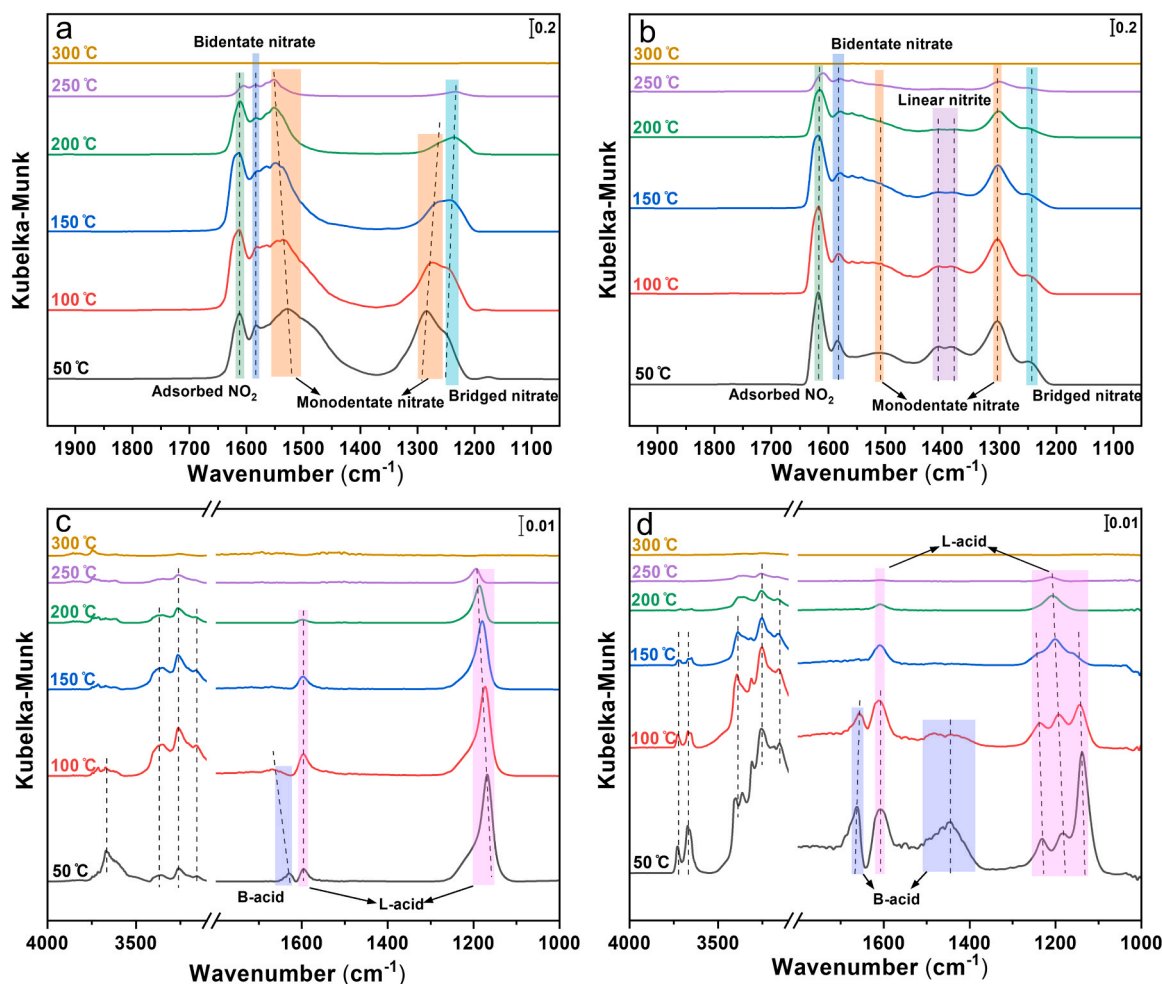


Fig. 6. In situ DRIFTS of NO+O<sub>2</sub> adsorption-desorption over CMT (a) and CMT-NT-C (b); in situ DRIFT spectra of NH<sub>3</sub> adsorption-desorption over CMT (c) and CMT-NT-C (d).



### 3.6.2. In situ DRIFTS of transient reaction

To further explore the reaction mechanism, in situ DRIFTS were carried out to study the transient reaction. Firstly, the in situ DRIFTS spectra of transient reaction between pre-adsorbed  $\text{NO} + \text{O}_2$  and  $\text{NH}_3$  were detected. As presented in Fig. 7(a,c), upon exposure to  $\text{NO} + \text{O}_2$  for 60 min at 200 °C, the adsorbed  $\text{NO}_2$  ( $1606\text{ cm}^{-1}$ ), bidentate nitrate ( $1580\text{ cm}^{-1}$ ), monodentate nitrate ( $1552\text{ cm}^{-1}$ ), linear nitrite ( $1381\text{ cm}^{-1}$ ), and bridged nitrate ( $1253\text{ cm}^{-1}$ ) species appeared on the CMT-NT-C

[8,19,52]. After introducing 500 ppm  $\text{NH}_3$ , the intensity of  $\text{NO}_x$  species gradually decreased followed by  $\text{NH}_3$  species generation within 30 min over the CMT-NT-C, whereas the bands belonged to linear nitrite shown almost no change in intensity over time. However, the adsorbed  $\text{NO}_x$  species on the CMT were marginally consumed after the introduction of  $\text{NH}_3$ , which was more slowly than that on the CMT-NT-C. It could be concluded that the  $\text{NO}$  removal could proceed via Langmuir-Hinshelwood (L-H) mechanism. And the normalized

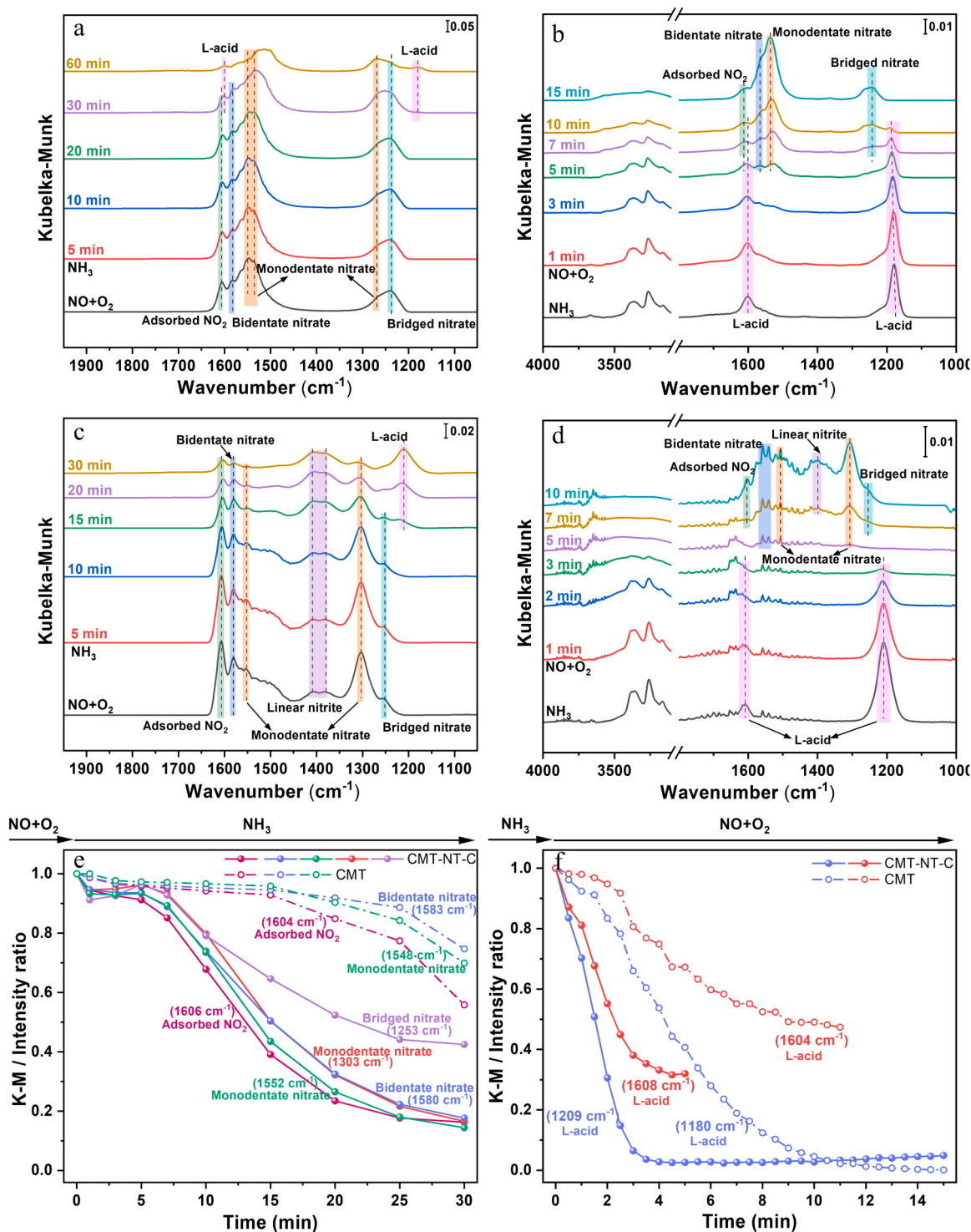


**Fig. 7.** In situ DRIFTS of the transient reactions at 200 °C between  $\text{NH}_3$  and pre-adsorbed  $\text{NO} + \text{O}_2$  over CMT (a) and CMT-NT-C (c); in situ DRIFTS of the transient reactions between  $\text{NO} + \text{O}_2$  and pre-adsorbed  $\text{NH}_3$  over CMT (b) and CMT-NT-C (d). Plots of the normalized intensity of adsorption species as a function of time after introducing  $\text{NH}_3$  (e) or  $\text{NO} + \text{O}_2$  (f).

intensities of adsorbed  $\text{NO}_x$  species as a function of time were recorded in Fig. 7e to clarify the consumption rate and reactivity of nitrate species. The consumption rate of adsorbed  $\text{NO}_2$  was the fastest on both the CMT and the CMT-NT-C, indicating that the adsorbed  $\text{NO}_2$  was the most active intermediate in the L-H mechanism [6]. Moreover, it was obviously found that the consumption rate of nitrate species on the CMT-NT-C was faster than that on the CMT, which testified that constructing hollow nanotube structure increased the reaction rate of the catalyst.

Furthermore, in situ DRIFTS studies were performed by switching the order of the introduction of the reactants. The catalysts were first exposed to 500 ppm  $\text{NH}_3$  at 200 °C for 60 min, and then the  $\text{NO} + \text{O}_2$  was introduced to react with the adsorbed  $\text{NH}_3$ . After the pre-adsorption of  $\text{NH}_3$ , several bands assigned to  $\text{NH}_4^+$  ( $1653 \text{ cm}^{-1}$ ) and coordinated  $\text{NH}_3$  ( $1608$  and  $1209 \text{ cm}^{-1}$ ) were observed on the CMT-NT-C (Fig. 7(d)). Upon introducing  $\text{NO} + \text{O}_2$ , the quick disappearance of  $\text{NH}_3$  species was accompanied by the formation of various  $\text{NO}_x$  species, and the adsorbed  $\text{NH}_3$  species on the CMT were also reactive with the introduction of  $\text{NO} + \text{O}_2$ , suggesting the  $\text{NO}$  removal also could be conducted on the catalysts via Eley-Rideal (E-R) mechanism [6,8,42]. According to the normalized intensities of adsorbed  $\text{NH}_3$  species as a function of time in Fig. 7f, the coordinated  $\text{NH}_3$  species disappear within 4 min in the CMT-NT-C and within 10 min in the CMT, implying the reaction rate of adsorbed  $\text{NH}_3$  species on the CMT-NT-C was much faster when exposed to  $\text{NO} + \text{O}_2$  compared to the CMT. These results demonstrated that the CMT-NT-C maintained a high reactivity of  $\text{NO}$  removal, which was due to the hollow nanotube structure accelerated the reaction rate of the reactants. In summary, the construction of hollow nanotube facilitated the  $\text{NO}$  removal reaction through either L-H or E-R mechanism.

### 3.6.3. Proposed reaction mechanism

Based on the above transient reaction results of in situ DRIFTS, it could be deduced that both the L-H and E-R mechanism could occur in the simultaneous removal of  $\text{NO}$  and  $\text{Hg}^0$ . Accordingly, the reaction rate between pre-adsorbed  $\text{NH}_3$  and  $\text{NO} + \text{O}_2$  or pre-adsorbed  $\text{NO} + \text{O}_2$  and  $\text{NH}_3$  was significantly faster after the formation of hollow nanotube. And to further prove it, the reaction rate of the prepared catalyst was calculated and shown in Fig. 8. It can be noticed that for either  $\text{NO}$  removal or  $\text{Hg}^0$  removal, the reaction rate values of CMT-NT-C are higher than those of CMT and CMT-NT, implying that the hollow nanotube catalysts accelerated the reaction rate of reactant molecules on the catalyst surface and improved its removal efficiency.

Combined with the literature [17,52,53] and above analysis, the

proposed reaction mechanism over the CMT-NT-C was depicted in Fig. 9. Firstly,  $\text{Hg}^0$  and  $\text{NH}_3$  were adsorbed on the surface of the catalyst, and the gas-phase oxygen was adsorbed on oxygen vacancy and was activated. Subsequently, the adsorbed  $\text{NH}_3$  was oxidized to  $\text{NH}_2$  species and  $\text{NH}$  species in turn, in which  $\text{NO}$  rapidly reacted with  $\text{NH}_2$  species and was finally reduced to  $\text{N}_2$ , which was carried out through the E-R mechanism. At the same time, part of  $\text{NO}$  was oxidized to adsorbed  $\text{NO}_2$  and nitrate species on the catalyst, and then reacted with adsorbed  $\text{NH}_3$  to form  $\text{N}_2$  and  $\text{H}_2\text{O}$ , which was carried out through the L-H mechanism. The formation of hollow nanotube ameliorated the redox equilibrium, thereby inhibiting the excessive oxidation of  $\text{NH}_3$  to  $\text{NH}$  species and reducing the production of  $\text{N}_2\text{O}$ . In addition, the adsorbed  $\text{Hg}^0$  simultaneously was oxidized by active oxygen species to generate  $\text{HgO}$ . Meanwhile, the active oxygen species consumed in the reaction process could be replenished by gas-phase oxygen in time to form a cycle. On the one hand, the formation of hollow nanotubes enhances the surface acidity, which facilitated the adsorption and activation of  $\text{NH}_3$  and thus improving the  $\text{NO}$  removal performance. On the other hand, the abundant oxygen vacancies on the CMT-NT-C enhanced the mobility of the lattice oxygen and generated more reactive oxygen species, which favored the adsorption and oxidation of  $\text{Hg}^0$  and accelerated the oxygen cycle during the reaction. Thus, the cooperation of surface acidity and oxygen vacancies on the hollow nanotube catalysts effectively improved the simultaneous removal of  $\text{NO}$  and  $\text{Hg}^0$ .

## 4. Conclusion

To conclude, the hollow nanotube Co-Mn/TiO<sub>2</sub> catalysts were fabricated from Co-Mn/TiO<sub>2</sub> nanoparticles precursor followed by hydrothermal method and found to display superior simultaneous removal performance for  $\text{NO}$  and  $\text{Hg}^0$ , giving above 98 %  $\text{NO}_x$  conversion with above 95 %  $\text{N}_2$  selectivity and nearly 100 %  $\text{Hg}^0$  removal efficiency in the range of 150–240 °C. It had been confirmed that the redox equilibrium was rationally ameliorated through the construction of hollow nanotube structure, which balanced the redox environmental requirements of  $\text{NO}$  and  $\text{Hg}^0$  well, thus allowing the catalysts to sustain the superior catalytic activity with high  $\text{N}_2$  selectivity. The promoted simultaneous removal performance of the CMT-NT-C was mainly attributed to: (1) the hollow nanotube structure possessed larger specific surface area, thus exposing more active sites; (2) the surface acidity of the catalyst was enhanced after the formation of hollow nanotube, facilitating the adsorption of reactants; (3) more oxygen vacancy was generated by constructing hollow nanotube, promoting the mobility of

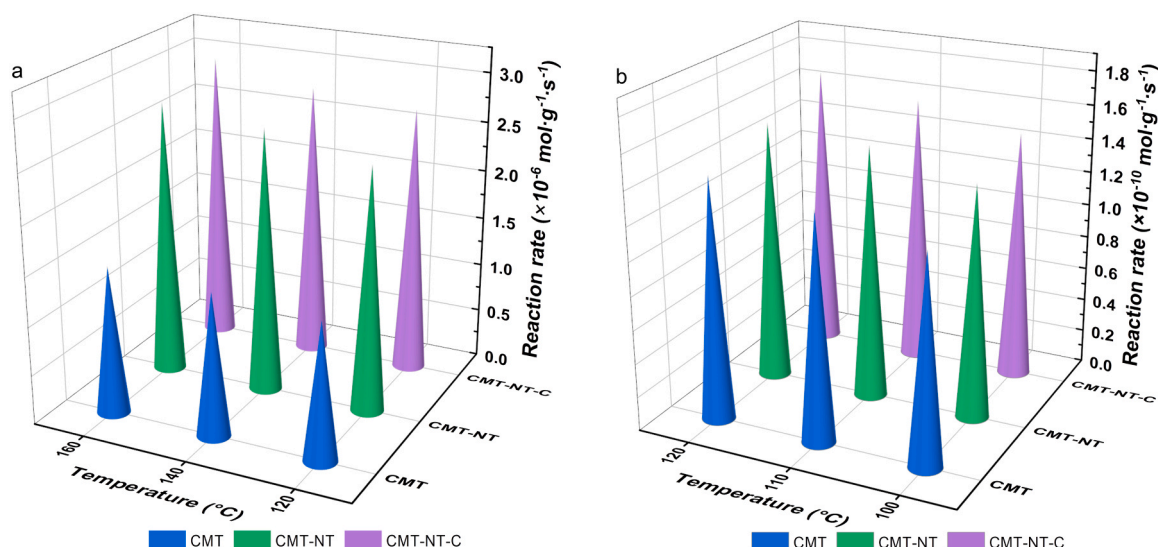


Fig. 8. The reaction rate versus temperatures for  $\text{NO}$  (a) and  $\text{Hg}^0$  (b).

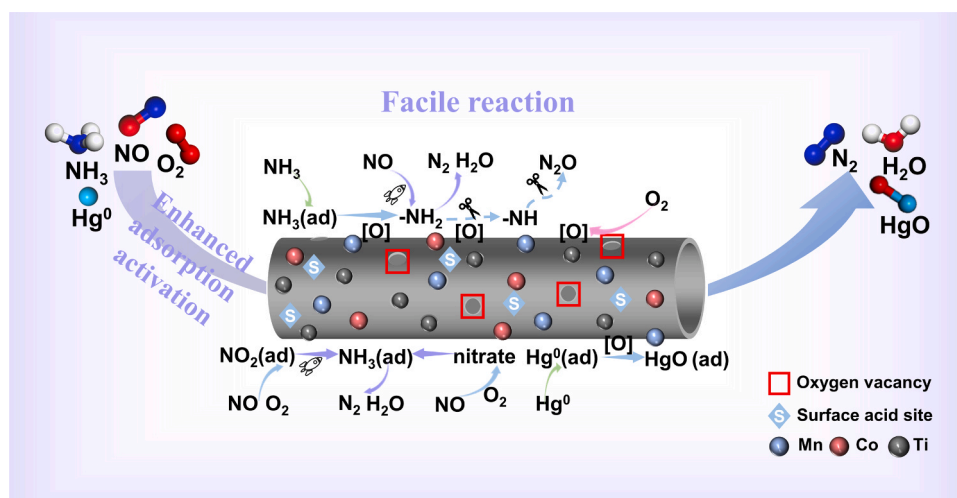


Fig. 9. The possible reaction mechanism for the simultaneous removal of NO and Hg<sup>0</sup> over the CMT-NT-C.

oxygen species. Therefore, the simultaneous removal performance of NO and Hg<sup>0</sup> was boosted via the synergistic effect of enhanced surface acidity and abundant oxygen vacancies on the hollow nanotube catalysts. Moreover, combined reaction mechanism analysis verifying that the reaction rate of reactants was obviously accelerated over the CMT-NT-C, which is one of the reasons that the low-temperature activity was improved by constructing the hollow nanotube structure. This study develops exceptionally efficient catalysts for simultaneous removal of NO and Hg<sup>0</sup>, and provides a promising strategy for engineering the simultaneous removal catalysts of NO and Hg<sup>0</sup> with excellent performance by constructing hollow nanoarchitectures.

#### CRediT authorship contribution statement

Biao Li: Conceptualization, Data curation, Formal analysis, Investigation, Methodology, Writing – original draft. Yaqin Hou: Funding acquisition, Supervision, Writing – review & editing. Jing Gao: Visualization, Writing – review & editing. Yifan Li: Formal analysis, Methodology. Bing Wang: Conceptualization, Formal analysis, Methodology. Zhanggen Huang: Conceptualization, Funding acquisition, Project administration, Resources, Supervision. Jiancheng Wang: Conceptualization, Funding acquisition, Project administration, Resources, Supervision. Liping Chang: Resources, Supervision. Kechang Xie: Resources, Supervision.

#### Declaration of Competing Interest

The authors declare that they have no known competing financial interests or personal relationships that could have appeared to influence the work reported in this paper.

#### Data Availability

Data will be made available on request.

#### Acknowledgements

This work was financially supported by the Strategic Priority Research Program of Chinese Academy of Sciences (No. XDA29020501), the National Natural Science Foundation of China (No. 21978314), the Key Laboratory of Coal Science and Technology (Taiyuan University of Technology), Ministry of Education (No. MKX202101), and ICC CAS SCJC-WRW-2022-20.

#### Appendix A. Supporting information

Supplementary data associated with this article can be found in the online version at [doi:10.1016/j.apcatb.2023.123353](https://doi.org/10.1016/j.apcatb.2023.123353).

#### References

- [1] L. Gao, C. Li, J. Zhang, X. Du, S. Li, J. Zeng, Y. Yi, G. Zeng, Simultaneous removal of NO and Hg<sup>0</sup> from simulated flue gas over CoO<sub>x</sub>-CeO<sub>2</sub> loaded biomass activated carbon derived from maize straw at low temperatures, *Chem. Eng. J.* 342 (2018) 339–349, <https://doi.org/10.1016/j.cej.2018.02.100>.
- [2] X. Du, C. Li, J. Zhang, Y. Zhu, C. Liang, L. Huang, K. Yang, C. Yao, Y. Ma, Tuning active oxygen species for boosting Hg<sup>0</sup> removal and SO<sub>2</sub>-resistance of Mn-Fe oxides supported on (NH<sub>4</sub>)<sub>2</sub>S<sub>2</sub>O<sub>8</sub> doping activated coke, *J. Hazard Mater.* 441 (2023), 129882, <https://doi.org/10.1016/j.jhazmat.2022.129882>.
- [3] J. Shi, J. Chen, S. Xiong, J. Mi, H. Liu, Z. Wang, H. Liu, J. Wang, J. Li, Structure-directing role of support on Hg<sup>0</sup> oxidation over V<sub>2</sub>O<sub>5</sub>/TiO<sub>2</sub> catalyst revealed for NO<sub>x</sub> and Hg<sup>0</sup> simultaneous control in an SCR reactor, *Environ. Sci. Technol.* 56 (2022) 9702–9711, <https://doi.org/10.1021/acs.est.2c01480>.
- [4] R. Hao, Z. Ma, Z. Zeng, Y. Mao, B. Yuan, L. Wang, Removal and recovery of gaseous elemental mercury using a Cl-doped protonated Polypyrrole@MWCNTs composite membrane, *Environ. Sci. Technol.* 56 (2022) 3689–3698, <https://doi.org/10.1021/acs.est.1c07594>.
- [5] L. Jia, Y. Yu, Z.P. Li, S.N. Qin, J.R. Guo, Y.Q. Zhang, J.C. Wang, J.C. Zhang, B. G. Fan, Y. Jin, Study on the Hg<sup>0</sup> removal characteristics and synergistic mechanism of iron-based modified biochar doped with multiple metals, *Bioresour. Technol.* 332 (2021), 125086, <https://doi.org/10.1016/j.biortech.2021.125086>.
- [6] Y. Wang, T. Shi, Q.-Y. Fan, Y. Liu, A. Zhang, Z. Li, Y. Hao, L. Chen, F. Liu, X. Gu, S. Zeng, Discovering surface structure and the mechanism of graphene oxide-triggered CeO<sub>2</sub>-WO<sub>3</sub>/TiO<sub>2</sub> catalysts for NO abatement with NH<sub>3</sub>, *ACS Catal.* 12 (2022) 8386–8403, <https://doi.org/10.1021/acscatal.2c01364>.
- [7] X. Qi, L. Han, J. Deng, T. Lan, F. Wang, L. Shi, D. Zhang, SO<sub>2</sub>-tolerant catalytic reduction of NO<sub>x</sub> via tailoring electron transfer between surface iron sulfate and subsurface ceria, *Environ. Sci. Technol.* 56 (2022) 5840–5848, <https://doi.org/10.1021/acs.est.2c00944>.
- [8] S. Xiong, Y. Peng, D. Wang, N. Huang, Q. Zhang, S. Yang, J. Chen, J. Li, The role of the Cu dopant on a Mn<sub>3</sub>O<sub>4</sub> spinel SCR catalyst: improvement of low-temperature activity and sulfur resistance, *Chem. Eng. J.* 387 (2020), 124090, <https://doi.org/10.1016/j.cej.2020.124090>.
- [9] Y. Xu, M. Zhou, M. Chen, Q. Zhang, L. Du, G. Luo, Simultaneous removal of NO and elemental mercury from coal-fired flue gas using natural ferruginous manganese ore at low temperature, *Fuel* 326 (2022), 125118, <https://doi.org/10.1016/j.fuel.2022.125118>.
- [10] W. Yang, X. Liu, X. Chen, Y. Cao, S. Cui, L. Jiao, C. Wu, C. Chen, D. Fu, I.D. Gates, Z. Gao, H.L. Jiang, A sulfur-tolerant MOF-based single-atom Fe catalyst for efficient oxidation of NO and Hg<sup>0</sup>, *Adv. Mater.* 34 (2022), e2110123, <https://doi.org/10.1002/adma.202110123>.
- [11] Y. Zhu, C. Li, Y. Lyu, S. Li, Y. Zhang, X. Du, Y. Zhai, Insight into the effect of SO<sub>2</sub> on the Hg<sup>0</sup> removal performance over a <sup>1</sup>V-<sup>8</sup>Ce/AC sorbent at low temperatures, *J. Hazard Mater.* 402 (2021), 123502, <https://doi.org/10.1016/j.jhazmat.2020.123502>.
- [12] Y. Chen, H. Li, J. Zhang, Y. Cao, J. Li, J. Yang, F. Li, C. Liu, Y. Wang, Y. Long, J. Hu, Enhanced performance and SO<sub>2</sub> tolerance of Ce modified TiO<sub>2</sub> supported Mn-Sm catalyst for synergistic removal of Hg<sup>0</sup> and NO from flue gas, *Fuel Process. Technol.* 227 (2022), 107136, <https://doi.org/10.1016/j.fuproc.2021.107136>.
- [13] H. Li, S. Wang, X. Wang, N. Tang, S. Pan, J. Hu, Catalytic oxidation of Hg<sup>0</sup> in flue gas over Ce modified TiO<sub>2</sub> supported Co-Mn catalysts: characterization, the effect



- of gas composition and co-benefit of NO conversion, *Fuel* 202 (2017) 470–482, <https://doi.org/10.1016/j.fuel.2017.04.071>.
- [14] X. Zhang, Y. Cui, J. Wang, B. Tan, C. Li, H. Zhang, G. He, Simultaneous removal of  $\text{Hg}^0$  and NO from flue gas by  $\text{Co}_{0.3}\text{-Ce}_{0.35}\text{-Zr}_{0.35}\text{O}_2$  impregnated with  $\text{MnO}_x$ , *Chem. Eng. J.* 326 (2017) 1210–1222, <https://doi.org/10.1016/j.cej.2017.06.014>.
- [15] H.L. Li, S.K. Wu, L.Q. Li, J. Wang, W.W. Ma, K.M. Shih,  $\text{CuO-CeO}_2/\text{TiO}_2$  catalyst for simultaneous NO reduction and  $\text{Hg}^0$  oxidation at low temperatures, *Catal. Sci. Technol.* 5 (2015) 5129–5138, <https://doi.org/10.1039/c5cy00794a>.
- [16] H. Zhang, Z. Li, T. Liu, M. Zhang, S. Deng, Y. Li, P. Liang, Satisfactory anti-interference and high performance of the  $1\text{Co-1Ce/Mn@ZSM-5}$  catalyst for simultaneous removal of NO and  $\text{Hg}^0$  in abominable flue gas, *Environ. Sci. Technol.* 56 (2022) 3596–3603, <https://doi.org/10.1021/acs.est.2c00143>.
- [17] B. Li, Y. Hou, Y. Li, K. Peng, Z. Huang, J. Wang, L. Chang, K. Xie, Synergistic removal of NO and  $\text{Hg}^0$  over Co-Mn/TiO<sub>2</sub> catalyst: high efficiency and in-depth reaction mechanism, *Fuel Process. Technol.* 240 (2023), 107578, <https://doi.org/10.1016/j.fuproc.2022.107578>.
- [18] Q. Zhao, B. Chen, J. Li, X. Wang, M. Crocker, C. Shi, Insights into the structure-activity relationships of highly efficient CoMn oxides for the low temperature  $\text{NH}_3$ -SCR of  $\text{NO}_x$ , *Appl. Catal. B: Environ.* 277 (2020), 119215, <https://doi.org/10.1016/j.apcatb.2020.119215>.
- [19] Z. Zhang, R. Li, M. Wang, Y. Li, Y. Tong, P. Yan, Y. Zhu, Two steps synthesis of  $\text{CeTiO}_x$  oxides nanotube catalyst: Enhanced activity, resistance of  $\text{SO}_2$  and  $\text{H}_2\text{O}$  for low temperature  $\text{NH}_3$ -SCR of  $\text{NO}_x$ , *Appl. Catal. B: Environ.* (2020), 119542, <https://doi.org/10.1016/j.apcatb.2020.119542>.
- [20] Q. Shi, B. Shen, X. Zhang, H. Lyu, J. Wang, S. Li, D. Kang, Insights into synergistic oxidation mechanism of  $\text{Hg}^0$  and chlorobenzene over  $\text{MnCo}_2\text{O}_4$  microsphere with oxygen vacancy and acidic site, *J. Hazard Mater.* 443 (2023), 130179, <https://doi.org/10.1016/j.jhazmat.2022.130179>.
- [21] H. Zhao, C.I. Ezech, S. Yin, Z. Xie, C.H. Pang, C. Zheng, X. Gao, T. Wu,  $\text{MoO}_3$ -adjusted  $\delta\text{-MnO}_2$  nanosheet for catalytic oxidation of  $\text{Hg}^0$  to  $\text{Hg}^{2+}$ , *Appl. Catal. B: Environ.* 263 (2020), 117829, <https://doi.org/10.1016/j.apcatb.2019.117829>.
- [22] Y. Zhu, C. Li, C. Liang, S. Li, X. Liu, X. Du, K. Yang, J. Zhao, Q. Yu, Y. Zhai, Y. Ma, Regulating  $\text{CeO}_2$  morphologies on the catalytic oxidation of toluene at lower temperature: a study of the structure–activity relationship, *J. Catal.* 418 (2023) 151–162, <https://doi.org/10.1016/j.jcat.2023.01.012>.
- [23] R. Mi, D. Li, Z. Hu, R.T. Yang, Morphology effects of  $\text{CeO}_2$  nanomaterials on the catalytic combustion of toluene: a combined kinetics and diffuse reflectance infrared fourier transform spectroscopy study, *ACS Catal.* 11 (2021) 7876–7889, <https://doi.org/10.1021/acscatal.1c01981>.
- [24] H. Zhu, X. Song, X. Han, X. Zhang, J. Bao, N. Zhang, G. He,  $\text{Co}_3\text{O}_4$  nanosheets preferentially growing (220) facet with a large amount of surface chemisorbed oxygen for efficient oxidation of elemental mercury from flue gas, *Environ. Sci. Technol.* 54 (2020) 8601–8611, <https://doi.org/10.1021/acs.est.0c03427>.
- [25] H. Sun, H. Wang, Z. Qu, Construction of  $\text{CuO/CeO}_2$  catalysts via the ceria shape effect for selective catalytic oxidation of ammonia, *ACS Catal.* 13 (2023) 1077–1088, <https://doi.org/10.1021/acscatal.2c05168>.
- [26] X. Hu, L. Huang, J. Zhang, H. Li, K. Zha, L. Shi, D. Zhang, Facile and template-free fabrication of mesoporous 3D nanosphere-like  $\text{Mn}_x\text{Co}_{3-x}\text{O}_4$  as highly effective catalysts for low temperature SCR of  $\text{NO}_x$  with  $\text{NH}_3$ , *J. Mater. Chem. A* 6 (2018) 2952–2963, <https://doi.org/10.1039/c7ta08000j>.
- [27] Y. Liao, K. Zhao, J. Yang, X. An, P. Zhang, Y. Dou, M. Zhao, D. Fu, Hetero-shelled hollow structure coupled with non-thermal plasma inducing spatial charge rearrangement for superior NO conversion and sulfur resistance, *Small* 18 (2022), e2106680, <https://doi.org/10.1002/smll.202106680>.
- [28] L. Chen, C. Zhang, Y. Li, C.-R. Chang, C. He, Q. Lu, Y. Yu, P. Duan, Z. Zhang, R. Luque, Hierarchically hollow  $\text{MnO}_2/\text{CeO}_2$  heterostructures for NO oxidation: remarkably promoted activity and  $\text{SO}_2$  tolerance, *ACS Catal.* 11 (2021) 10988–10996, <https://doi.org/10.1021/acscatal.1c01578>.
- [29] S. Zhang, T. Hedtke, L. Wang, X. Wang, T. Cao, M. Elimelech, J.H. Kim, Engineered nanoconfinement accelerating spontaneous manganese-catalyzed degradation of organic contaminants, *Environ. Sci. Technol.* 55 (2021) 16708–16715, <https://doi.org/10.1021/acs.est.1c06551>.
- [30] M.X. Gu, L.P. Gao, S.S. Peng, S.C. Qi, X.B. Shao, X.Q. Liu, L.B. Sun, Transition metal single atoms constructed by using inherent confined space, *ACS Nano* 17 (2023) 5025–5032, <https://doi.org/10.1021/acsnano.2c12817>.
- [31] X. Chen, P. Wang, P. Fang, H. Wang, C. Cen, W. Zeng, Z. Wu, Design strategies for SCR catalysts with improved  $\text{N}_2$  selectivity: the significance of nano-confining effects by titanate nanotubes, *Environ. Sci.: Nano* 4 (2017) 437–447, <https://doi.org/10.1039/c6en00627b>.
- [32] Y. Sun, S. Xu, B. Bai, L. Li, Y. Kang, X. Hu, Z. Liao, C. He, Bi-template fabrication of hollow tubular  $\text{Ce}_x\text{Sr}_{1-x}\text{TiO}_3$  with regulable surface acidity and oxygen mobility for efficient destruction of chlorobenzene: intrinsic synergy effect and reaction mechanism, *Environ. Sci. Technol.* 56 (2022) 5796–5807, <https://doi.org/10.1021/acs.est.2c00270>.
- [33] L. Ye, P. Lu, Y. Xianhui, H. Huang, Boosting simultaneous catalytic removal of  $\text{NO}_x$  and toluene via cooperation of Lewis acid and oxygen vacancies, *Appl. Catal. B: Environ.* 331 (2023), 122696, <https://doi.org/10.1016/j.apcatb.2023.122696>.
- [34] B. Dong, Y. Pei, F. Zhao, T.W. Goh, Z. Qi, C. Xiao, K. Chen, W. Huang, N. Fang, In situ quantitative single-molecule study of dynamic catalytic processes in nanoconfinement, *Nat. Catal.* 1 (2018) 135–140, <https://doi.org/10.1038/s41929-017-0021-1>.
- [35] Z. Xu, S. Impeng, X. Jia, F. Wang, Y. Shen, P. Wang, D. Zhang,  $\text{SO}_2$ -Tolerant catalytic reduction of  $\text{NO}_x$  by confining active species in  $\text{TiO}_2$  nanotubes, *Environ. Sci.: Nano* 9 (2022) 2121–2133, <https://doi.org/10.1039/d2en00144f>.
- [36] D. Meng, Q. Xu, Y. Jiao, Y. Guo, Y. Guo, L. Wang, G. Lu, W. Zhan, Spinel structured  $\text{Co}_3\text{Mn}_2\text{O}_x$  mixed oxide catalyst for the selective catalytic reduction of  $\text{NO}_x$  with  $\text{NH}_3$ , *Appl. Catal. B: Environ.* 221 (2018) 652–663, <https://doi.org/10.1016/j.apcatb.2017.09.034>.
- [37] S. Rong, P. Zhang, F. Liu, Y. Yang, Engineering crystal facet of  $\alpha\text{-MnO}_2$  nanowire for highly efficient catalytic oxidation of carcinogenic airborne formaldehyde, *ACS Catal.* 8 (2018) 3435–3446, <https://doi.org/10.1021/acscatal.8b00456>.
- [38] D. Damma, D.K. Pappas, T. Boningari, P.G. Smirniotis, Study of Ce, Sb, and Y exchanged titania nanotubes and superior catalytic performance for the selective catalytic reduction of  $\text{NO}_x$ , *Appl. Catal. B: Environ.* 287 (2021), 119939, <https://doi.org/10.1016/j.apcatb.2021.119939>.
- [39] R.-R. Ding, W.-Q. Li, C.-S. He, Y.-R. Wang, X.-C. Liu, G.-N. Zhou, Y. Mu, Oxygen vacancy on hollow sphere  $\text{CuFe}_2\text{O}_4$  as an efficient Fenton-like catalysis for organic pollutant degradation over a wide pH range, *Appl. Catal. B: Environ.* 291 (2021), 120069, <https://doi.org/10.1016/j.apcatb.2021.120069>.
- [40] S. Zhang, Y. Zhao, J. Yang, J. Zhang, C. Zheng, Fe-modified  $\text{MnO}_x/\text{TiO}_2$  as the SCR catalyst for simultaneous removal of NO and mercury from coal combustion flue gas, *Chem. Eng. J.* 348 (2018) 618–629, <https://doi.org/10.1016/j.cej.2018.05.037>.
- [41] Y. Xu, X. Wu, L. Cao, Y. Ma, R. Ran, Z. Si, D. Weng, Z. Ma, B. Wang, Crystal orientation-dependent activity of tungsten-based catalysts for selective catalytic reduction of NO with  $\text{NH}_3$ , *J. Catal.* 375 (2019) 294–303, <https://doi.org/10.1016/j.jcat.2019.06.012>.
- [42] F. Wang, P. Wang, T. Lan, Y. Shen, W. Ren, D. Zhang, Ultralow-temperature  $\text{NO}_x$  reduction over  $\text{SmMn}_2\text{O}_5$  mullite catalysts via modulating the superficial dual-functional active sites, *ACS Catal.* 12 (2022) 7622–7632, <https://doi.org/10.1021/acscatal.2c01897>.
- [43] L. Li, J.-W. Shi, M. Tian, C. Chen, B. Wang, M. Ma, C. He, In situ fabrication of robust three dimensional ordered macroporous  $\gamma\text{-MnO}_2/\text{LaMn}_{0.35}\text{O}_{1.5}$  catalyst for chlorobenzene efficient destruction, *Appl. Catal. B: Environ.* 282 (2021), 119565, <https://doi.org/10.1016/j.apcatb.2020.119565>.
- [44] W.L. Wang, Q. Meng, Y. Xue, X. Weng, P. Sun, Z. Wu, Lanthanide perovskite catalysts for oxidation of chloroaromatics: Secondary pollution and modifications, *J. Catal.* 366 (2018) 213–222, <https://doi.org/10.1016/j.jcat.2018.07.022>.
- [45] Y. Fang, Q. Zhang, H. Zhang, X. Li, W. Chen, J. Xu, H. Shen, J. Yang, C. Pan, Y. Zhu, J. Wang, Z. Luo, L. Wang, X. Bai, F. Song, L. Zhang, Y. Guo, Dual activation of molecular oxygen and surface lattice oxygen in single atom  $\text{Cu}_1/\text{TiO}_2$  catalyst for CO oxidation, *Angew. Chem. Int. Ed. Engl.* 61 (2022), e202212273, <https://doi.org/10.1002/anie.202212273>.
- [46] L. Nie, D. Mei, H. Xiong, B. Peng, Z. Ren, X.I.P. Hernandez, A. DeLaRiva, M. Wang, M.H. Engelhard, L. Kovarik, A.K. Datye, Y. Wang, Activation of surface lattice oxygen in single-atom Pt/CeO<sub>2</sub> for low-temperature CO oxidation, *Science* 358 (2017) 1419–1423, <https://doi.org/10.1126/science.aao2109>.
- [47] X. Yang, F. Li, W. Liu, L. Chen, J. Qi, W. Sun, F. Pan, T. Duan, F. Sun, Oxygen vacancy-induced spin polarization of tungsten oxide nanowires for efficient photocatalytic reduction and immobilization of uranium(VI) under simulated solar light, *Appl. Catal. B: Environ.* 324 (2023), 122202, <https://doi.org/10.1016/j.apcatb.2022.122202>.
- [48] S. Zhao, Y. Yang, F. Bi, Y. Chen, M. Wu, X. Zhang, G. Wang, Oxygen vacancies in the catalyst: Efficient degradation of gaseous pollutants, *Chem. Eng. J.* 454 (2023), 140376, <https://doi.org/10.1016/j.cej.2022.140376>.
- [49] S. Cai, T. Xu, P. Wang, L. Han, S. Impeng, Y. Li, T. Yan, G. Chen, L. Shi, D. Zhang, Self-protected  $\text{CeO}_2\text{-SnO}_2/\text{SO}_4^{2-}/\text{TiO}_2$  catalysts with extraordinary resistance to alkali and heavy metals for  $\text{NO}_x$  reduction, *Environ. Sci. Technol.* 54 (2020) 12752–12760, <https://doi.org/10.1021/acs.est.0c04911>.
- [50] J. Fan, P. Ning, Y. Wang, Z. Song, X. Liu, H. Wang, J. Wang, L. Wang, Q. Zhang, Significant promoting effect of Ce or La on the hydrothermal stability of Cu-SAPO-34 catalyst for  $\text{NH}_3$ -SCR reaction, *Chem. Eng. J.* 369 (2019) 908–919, <https://doi.org/10.1016/j.cej.2019.03.049>.
- [51] B. Wang, M. Wang, L. Han, Y. Hou, W. Bao, C. Zhang, G. Feng, L. Chang, Z. Huang, J. Wang, Improved activity and  $\text{SO}_2$  resistance by Sm-modulated redox of  $\text{MnCeSmTiO}_x$  mesoporous amorphous oxides for low-temperature  $\text{NH}_3$ -SCR of NO, *ACS Catal.* 10 (2020) 9034–9045, <https://doi.org/10.1021/acscatal.0c02567>.
- [52] W. Chen, S. Yang, H. Liu, F. Huang, Q. Shao, L. Liu, J. Sun, C. Sun, D. Chen, L. Dong, Single-atom Ce-modified  $\alpha\text{-Fe}_2\text{O}_3$  for selective catalytic reduction of NO with  $\text{NH}_3$ , *Environ. Sci. Technol.* 56 (2022) 10442–10453, <https://doi.org/10.1021/acs.est.2c02916>.
- [53] Y. Yang, J. Liu, J. Ding, Y. Yu, J. Zhang, Mercury/oxygen reaction mechanism over  $\text{CuFe}_2\text{O}_4$  catalyst, *J. Hazard Mater.* 424 (2022), 127556, <https://doi.org/10.1016/j.jhazmat.2021.127556>.